Imaging local pH in boundary layers at 3D electrodes in electrochemical flow systems

Ligthart, Nathalie E.G.; Sommer, Julius; Bleeker, Jorrit; Baumgartner, Lorenz M.; Padding, Johan T.; Vermaas, David A.

DOI
10.1016/j.cej.2025.160474

Publication date
2025

Document Version
Final published version

Published in
Chemical Engineering Journal

Citation (APA)
Ligthart, N. E. G., Sommer, J., Bleeker, J., Baumgartner, L. M., Padding, J. T., & Vermaas, D. A. (2025). Imaging local pH in boundary layers at 3D electrodes in electrochemical flow systems. *Chemical Engineering Journal*, *507*, Article 160474. https://doi.org/10.1016/j.cej.2025.160474

Chemical Engineering Journal 507 (2025) 160474

Contents lists available at ScienceDirect

Chemical Engineering Journal

journal homepage: www.elsevier.com/locate/cej

Imaging local pH in boundary layers at 3D electrodes in electrochemical flow systems

Nathalie E.G. Ligthart [a,1,2], Julius Sommer [a,1,3], Jorrit Bleeker [a,4], Lorenz M. Baumgartner [a,5], Johan T. Padding [b,6], David A. Vermaas [a,7,*]

[a] Department of Chemical Engineering, Delft University of Technology, Delft, the Netherlands
[b] Department of Process and Energy, Delft University of Technology, Delft, the Netherlands

ARTICLE INFO

Keywords:
FLIM
Boundary layer
pH imaging
3D electrodes
Electrochemical conversion

ABSTRACT

Electrochemical reactors, such as water electrolyzers, CO_2 electrolyzers, fuel cells, and flow batteries, will be essential in electrifying industry as part of the global transition towards a defossilized and sustainable economy. These technologies require further optimization to enhance efficiency and reduce costs for widespread adoption. Hydrodynamics and mass transfer at electrode–electrolyte interfaces significantly affect electrochemical conversion reactions by influencing the reactant availability and pH in the local reaction environment. 3D electrodes, such as flow-through foams and suspension electrodes, hold a great advantage over 2D electrodes as they moderate pH changes and reactant depletion by spreading the current over a larger electrode area and electrolyte volume. We study the diffusion boundary layer in operando around a single mm-sized particle, representing an element of a 3D electrode. We visualize the local and transient pH with Fluorescence Lifetime Imaging Microscopy (FLIM) during H_2O reduction at various current densities and electrolyte flow velocities at a resolution down to 9 μm and 2 Hz. In addition, we apply an intermittent current to investigate how long the capacitive electric double layer of a suspension electrode particle can maintain an electrochemical reaction during their time of non-contact with a current collector, mimicking applications with Faradaic charge transfer (*i.e.* flow batteries, microbial fuel cells, capacitance-based electrolyzers). We demonstrate that the diffusion boundary layer is not symmetrical, but depend on the direction of the electric field, the current density and the flow conditions. The substantial pH gradients and boundary layer formation at the scale of hundreds of micrometers underline the importance of controlling flow in or around electrodes, making 3D electrodes an important asset for creating suitable reaction conditions in mass transport-limited electrochemical conversions.

1. Introduction

Developing technologies for sustainable production methods in the chemical industry is essential in the energy transition and decarbonization of industry [1,2]. Electrochemical processes are gaining interest as alternatives to thermochemical routes, for example to synthesize high-value chemicals and fuels from renewable energy sources and captured CO_2 [3]. Base materials such as syngas, formic acid, and ethylene are produced in CO_2 electrolyzers as intermediates and are processed further to obtain the essential hydrocarbons without using fossil fuels as carbon source [4,5]. Additional electrochemical reactor applications include technologies for hydrogen [6,7], salinity gradient energy [8], energy storage [9,10], carbon capture [11,12], and wastewater treatment [13–16]. Although these electrochemical technologies

* Corresponding author at: Department of Chemical Engineering, Delft University of Technology, 2629 HZ Delft, The Netherlands.
E-mail address: d.a.vermaas@tudelft.nl (D.A. Vermaas).
[1] Co-first author.
[2] orcid.org/0009-0004-5594-2190.
[3] orcid.org/0009-0003-4399-9934.
[4] orcid.org/0000-0002-8275-7693.
[5] orcid.org/0000-0002-6745-765X.
[6] orcid.org/0000-0003-4161-0748.
[7] orcid.org/0000-0002-4705-6453.

https://doi.org/10.1016/j.cej.2025.160474
Received 19 November 2024; Received in revised form 27 January 2025; Accepted 8 February 2025
Available online 16 February 2025

are promising, high costs, low efficiency, and poor stability pose considerable challenges for large-scale application of electrochemical reactors [4,17].

Working at high current density while maintaining high product selectivity and long-term stability is challenging, but essential for realizing economic viability of many of these new technologies. High current densities can cause severe local concentration gradients (or depletion) of redox active species with low solubility and can negatively affect product selectivity and catalyst stability [18,19]. In case of proton-coupled electron transfer reactions, this causes local pH gradients, which can hamper the reaction efficiency. Therefore, fast mass transport is extremely important to counter depletion and loss of selectivity. In particular, regarding the example of electrochemical CO_2 reduction, the selectivity towards carbonaceous products critically depends on maintaining a narrow pH window of 7–8 near the electrode [20] to suppress the Hydrogen Evolution Reaction (HER) [18,21,22]. Just like other proton-coupled electron transfer reactions, CO_2 reduction suffers from considerable energy and selectivity losses when the pH at the surface is higher, because the high pH raises the Nernst potential and shifts the equilibrium of dissolved CO_2 towards (bi)carbonate [21,23,24]. Hence, understanding mass transport and pH profiles is essential to limit performance loss during operation at high current densities.

However, direct measurements of local concentrations are sparse, and limited to flat sheets or gas diffusion electrodes [25–27]. The electrode geometry is pivotal for the development of diffusion boundary layer and the pH profile near the electrode. 3D electrodes, which can be flow-through electrodes such as foams or suspension electrodes, hold a clear advantage over flat electrodes in this regard, because 1) they spread the current over a larger electrode area and electrode volume, moderating the local current density and surface pH [28,29], and 2) they disrupt the flow to prevent diffusion boundary layers from developing over the length of the electrode. A continuously undeveloped diffusion boundary layer improves mass transport, which is reflected in higher Sherwood numbers [30]. Flow-through electrodes are a popular choice for a variety of applications, including water electrolysis and CO_2 electrolysis [28,31,32], and flowable suspension electrodes (sometimes referred to as slurry electrodes) have been found especially effective in Flow electrode Capacitive Deionization (FCDI) [33,34], Electrochemical Flow Capacitors (EFCs) [35,36], Redox Flow Batteries (RFBs) [9,37], and microbial fuel cells (MFCs) [38,39]. However, these previous works on 3D electrodes have focused on studying the performance parameters (such as power density and removal efficiency), without detailed insight in the local reaction conditions. At the same time, 3D electrodes feature strongly heterogeneous flow and concentration fields, where the diffusion boundary layer develops under flow around an electrode segment (filaments in case of flow through, particles in case of a suspension). Hence, we need to further understand the local reaction conditions in 3D electrodes and the extent to which the capacitance contributes to electrochemical conversion in suspension electrodes.

Therefore, in this work we investigate the local pH at the electrode–electrolyte interface of a reactive particle representing an element in a 3D electrode, and we evaluate the Faradaic contribution during the discharge of a capacitive particle. We inserted a single Activated Carbon (AC) particle electrode in an electrolytic flow cell and imaged the local pH with Fluorescent Lifetime Imaging Microscopy (FLIM) [21,40] under various current densities and flow conditions relevant for a particle in a flowing suspension. We determine the pH around the particle electrode and use the resulting OH^- concentration to extract the diffusion boundary layer thickness in all directions around the single-particle electrode during H_2O reduction as a model reaction.

In contrast to elements in a flow-through electrode, particles in a flowing suspension are not continuously in contact with a current source, but rather pick up electrons during collisions with dynamic networks and experience an intermittent current supply. We investigate whether the particle's electric double layer capacitance can maintain the ongoing Faradaic reaction long enough to mitigate the non-contact time by combining the FLIM and potentiostat data and fitting the discharge curve to a self-discharge model of Electric Double Layer Capacitors (EDLCs) [41]. This allows to elucidate how often suspension particles should reestablish electrical contact to overcome the challenges of their low conductivity [34,35,42].

Our findings can be extended towards other pH-sensitive reactions and different 3D electrode geometries, and are equally applicable to other mass transfer-limited reactions. We consider the OH^- produced during H_2O reduction as a proxy for local generation of electrolysis products and depletion of reactants, which can be used as a model for aqueous-based proton-coupled electron transfer reactions. Please note that our work focuses on flow around 3D electrode elements (such as flow-through foam filaments or particles in suspension electrodes), as flow-by configurations and membrane-electrode assemblies present a significantly different environment. Furthermore, our findings on particle capacitance as electron supply during Faradaic reactions are applicable to suspension electrode applications and aid in the design of current collectors and non-contact time of the particles.

2. Methods

A large AC particle (455 ± 23 μm radius, Norit 18x40 AG 1, Cabot) was chosen to match the type of AC particles typically used in suspension electrodes, albeit larger in size. The selection was based on its large porous surface area, suitable for capacitance experiments. The particle was affixed to the tip of a hardened steel needle using electrically conductive epoxy adhesive (Eccobond 56C). The needle and epoxy were coated with an insulating acrylic layer (nail polish) to prevent contact with the electrolyte. The AC particle electrode was placed as cathode in a two-compartment electrochemical flow cell as shown in Fig. 1. The cell was equipped with an Ag/AgCl reference electrode (LF-1-45, Alvatek) and nickel plate (Ni-plate) anode. The channels were separated by a Cation Exchange Membrane (CEM, Selemion CMV). The anolyte consisted of 0.1 M KOH in deionized water. The catholyte consisted of 0.1 M K_2SO_4 and 0.1 mM of fluorescent quinolinium-based dye (see Fig. S3a) [21,40]. The pH-sensitive fluorescence lifetime of this dye allows for pH measurements between pH 7 to 13 (see Fig. S3b). The electrolytes were pumped through the cell at flow velocities ranging from 0.1 to 2.1 mm/s by two syringe pumps and collected in waste containers to create a single-pass system. All experiments were performed at constant currents between 0 and −143 mA/g carbon (corresponding to 0 to −106 mA/cm^2, based on the geometric surface area of the particle) applied by a Vertex.100 mA potentiostat (±100 mA/±10 V, Ivium). To mitigate long-term issues such as corrosion and bubble entrapment, each single-particle electrode was used for a maximum of 40 min total runtime with minimal current application, and equilibration effects such as adsorption were addressed by flowing the catholyte over the particle for at least 60 s before measurements. See section 1.1 of the SI for more information on the setup and dye.

FLIM was performed in-situ with a light microscope equipped with a 2.5× objective, 405 nm diode laser (20 MHz, 300 mW), a spinning disc confocal imager (X-Light V2, Crest Optics) and a FLIM Toggel camera (512 × 470 pixels, Lambert Instruments) resulting in a pH map with a pixel size of 9 μm. The microscope setup and calibration of dyes are described in more detail in section 1.1 of the SI and Ref. [21,40]. The images were recorded in LIFA 1.4 software (Lambert Instruments) and processed further with an in-house developed Python script, as described in section 1.2 of the SI.

The formation and growth of the boundary layer in no-flow conditions were recorded at −43 mA/g (–32 mA/cm^2) for 150 s, with one FLIM image recorded every 0.5 s (2 Hz). To reduce noise, a running average over 3 images was used during data processing. We characterize each experiment using the Fourier number (*Fo*), given by [43]

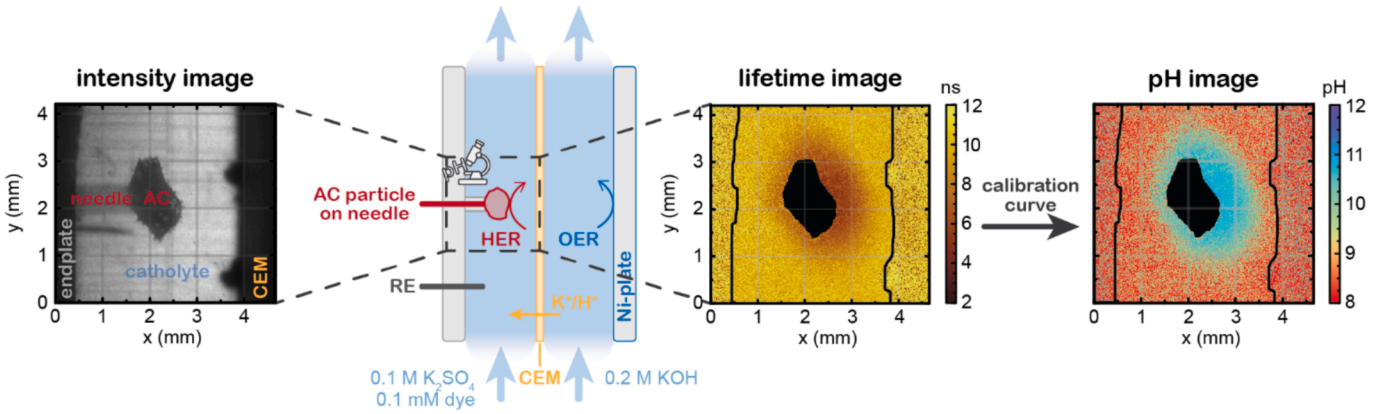

Fig. 1. Schematic of the single activated carbon (AC) particle electrode inside the electrochemical flow cell and the microscope imaging window. The local fluorescence intensity and lifetime of the added pH-sensitive dye are recorded. The fluorescence lifetime image is converted to a pH map, using the calibration curve shown in the SI (section 1.1).

$$Fo = \frac{t}{t_D} = \frac{tD_{OH^-}}{L^2} \quad (1)$$

in which t is the measurement time, t_D and D_{OH^-} are the diffusion timescale and the diffusion coefficient of OH^-, respectively, and we consider half the channel depth (approx. 1.8 mm) as the characteristic length scale (L). *Fo* gives the relative significance of the diffusion length of OH^- (numerator) versus the distance to a wall (denominator) during the transient measurement.

The influence of current and flow velocity were both studied in steady state conditions. The conditions of interest were applied for 60 s and the local pH was recorded with FLIM at a lower frequency of 1 Hz. The first 40 s were used to reach steady state, and the last 20 s were averaged to yield the results. The current density was varied between 0 and −143 mA/g (−106 mA/cm^2) at a constant flow velocity of 0.3 mm/s. Influence of flow velocity was investigated between 0.1 and 2.1 mm/s, at a constant current density of −15 mA/g (−11 mA/cm^2). These flow velocities represent the velocity in a flow-through electrode or the relative velocity between particle and solution in a suspension electrode. We note that higher flow velocities are used in flow-by configurations, which are out of scope for this work. We define the Reynolds (*Re*) number as

$$Re = \frac{uL}{\nu} \quad (2)$$

with u being the channel-averaged flow velocity, ν the kinematic viscosity of the liquid phase, and L the characteristic length, for which the particle diameter (d_p) is inserted to arrive at the particle Reynolds number (Re_p).

OH^- concentration gradients were modelled around a spherical particle inside a 2D flow channel in *COMSOL Multiphysics 6.1* for comparison with our experimental results. The geometry was designed to resemble the experimental setup, with a ratio between the particle diameter and channel width similar to the experiments, and an imposed electrical field perpendicular to the electrolyte flow direction. See section 1.3 of the SI for further details.

3. Results and discussion

We used FLIM to record how the concentration boundary layer develops over time, and how it depends on current density and electrolyte flow velocity. Our results confirm established theories, but also show unexpected behavior. Please note that, unlike previous pH mapping with FLIM [21], the current setup with a reactive particle in the middle of the flow channel has no interference from gaskets or walls, which allows us to measure the local pH very close to the reaction site.

3.1. Boundary layer and plume formation

In the simplest case, we apply a low constant current (−43 mA/g, –32 mA/cm^2) without convection by applied flow or detaching hydrogen bubbles. As expected, a region with increased pH, that corresponds to the diffusion boundary layer, forms after starting the current and grows significantly over time (see Fig. 2a-e) as OH^- is produced and transported away from the electrode surface by migration and diffusion. The placement of the anode on the right side of the particle causes a stronger electric field and increased local ionic current density (j_L), with a higher ion flux, on the right side of the particle (see Fig. 2f for a modeled spherical particle electrode). The asymmetrical system, in combination with migration in the direction of the membrane and the irregular shape of the electrode, causes the boundary layer to grow asymmetrically, with a thicker layer on the side of the particle that is facing the anode (see Fig. 2c-e). The buildup of OH^- ions is analogous to consumption of reactants, and should be considered when performing pH-sensitive reactions or when working with poorly soluble reagents.

We processed the measured pH maps to obtain a more quantitative analysis of the boundary layer thickness (δ) by casting rays from the exterior of the particle into the electrolyte and extracting the boundary layer thickness along each ray. The rays were cast at a slightly modified angle from the exterior normal, as described in section 1.2 of the SI, to prevent excessive crossing of the rays. Fig. 3a shows the particle electrode with several rays (A, B, C, and D) and their mirror images (A', B', C', and D'). We fit a linear graph to the difference between the bulk- and local OH^- concentration (ΔC_{OH^-}) in the region close to the particle and define the x-intercept as the diffusion boundary layer thickness. This is shown for ray C at three different times (t_1, t_2, and t_3) in Fig. 3b. For the rays A, B, C, D (and their mirror images), the estimated boundary layer thickness is indicated by a colored dot in Fig. 3a. The white dots indicate the end of the boundary layer on all rays in between those shown in this figure. The analysis is performed over 360 rays in total. A more thorough explanation on the ray casting and data processing is provided in section 1.2 of the SI.

As a result, we can monitor the diffusion boundary layer thickness along any ray over time. The results are shown in Fig. 3c for rays B, C, and D (solid lines), and the mirrored counterparts B', and D' (dashed lines). C' is not included because of interference by the needle placement. The larger diffusion boundary layer thickness along rays B, C, and D compared to the mirrored counterparts B' and D' confirms that the development of the diffusion boundary layer around the particle is asymmetrical and depends on the location relative to the anode. During this experiment without electrolyte flow, the diffusion boundary layer thickness is eventually limited by the size of the channel. It reaches as far as the membrane (black line in Fig. 3a) along rays C and D after

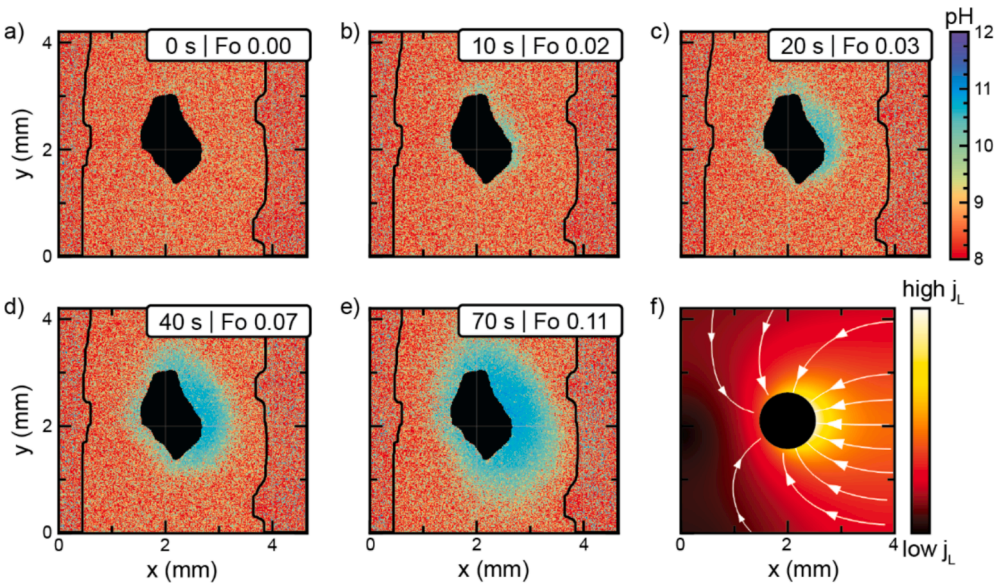

Fig. 2. a-e) Development of the pH around an ac particle electrode through time at a current of −43 mA/g (–32 mA/cm^2) in the absence of flow and rising bubbles, as recorded with our FLIM setup. The region with increased pH marks the diffusion boundary layer. f) Modeled electric field lines and resulting local current density in the electrolyte (j_L) around a spherical particle electrode in a similar flow channel. The asymmetry of the system results in a stronger electric field at the right side of the particle electrode, with a higher ion flux in that region. Fo is the dimensionless Fourier number defined by eq. (1).

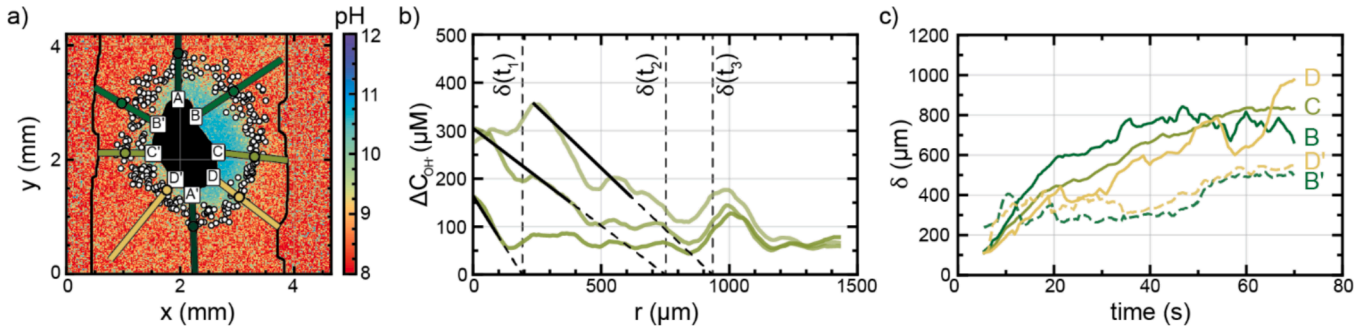

Fig. 3. a) Colour map of the measured pH after 40 s of applying −43 mA/g (–32 mA/cm^2) without flowing the electrolyte. Rays are casted from the particle surface and the boundary layer thickness is estimated along each ray. Several rays (A, B, C, D) and their respective mirror images (A', B', C', and D') are shown with the edge of the diffusion boundary layer indicated with a coloured dot. The white dots indicate the estimated boundary layer thickness along all rays in between. b) Visualization of the boundary layer thickness (δ) along ray C (at $t_1 = 9$ s, $t_2 = 50$ s, and $t_3 = 68$ s), by finding the x-intercept of the linearized $\Delta C_{OH^-}(r) = C_{bulk} - C(r)$ gradient near the particle. c) Development of the boundary layer thickness through time on rays B, C, and D, and the mirrored counterparts B' and D'.

approximately 90 s, as can be seen in Fig. S8 in the SI, and cannot grow further as a result.

The boundary layer grows roughly sublinear for the first 50 s, when the channel walls are not limiting yet and $Fo < 0.08$. Although the boundary layer growth in this case is subject to mixed migration and diffusion transport in the asymmetric system, this duration is close to the timescale that would be expected from penetration theory ($Fo = 0.1$ at $t = 60$ s).

The situation changes drastically when introducing flow. Introducing a mild upward flow (0.3 mm/s, $Re_p = 0.27$) significantly diminishes the diffusion boundary layer along the sides of the particle (Fig. 4b) versus the previous case without convection (Figs. 2 and 3). Instead of forming a thick pH gradient in the x-direction, most produced OH^- gets flushed upward to form a plume above the particle electrode (indicated with arrow 3 in Fig. 4c). In addition, FLIM reveals OH^- accumulation near the membrane due to concentration polarization (arrow 1, Fig. 4a), and H_2 bubble formation is visible as well (arrow 2, Fig. 4c).

In our system (HER), the plume signifies a region with increased pH, but more generally it indicates a region with altered reaction conditions. This can constitute anything from altered pH for proton-coupled electron transfer reactions, to reactant depletion for other reaction types. Ideally, the plume should be dissipated before the next active electrode section is reached, such as a strut in a porous (foam) electrode or a particle in a suspension electrode, to maintain a suitable reaction environment on the microscale. This is also important to prevent accumulation of changing conditions through the height of the electrode channel. For a porous electrode, this can result in a larger optimal pore size in the y-direction, and for suspension electrodes this can result in larger optimal spacing between the suspended particles.

To allow a 3D electrode with a large surface area (thus relatively small distance between the struts or particles) while minimizing plume effects, both the applied current density and flow velocity can be varied to reduce the size of the resulting plume. While higher current densities promote the plume formation and cause a steep pH gradient in the diffusion boundary layer (Fig. 4a-c), higher flowrates help repress these effects (Fig. 4d-f). Increasing the flow velocity diminishes the boundary layer and dissipates the plume at a shorter length scale, which in turn allows for smaller pores or loading more active particles in the same geometrical area and using them effectively. Because electrochemical

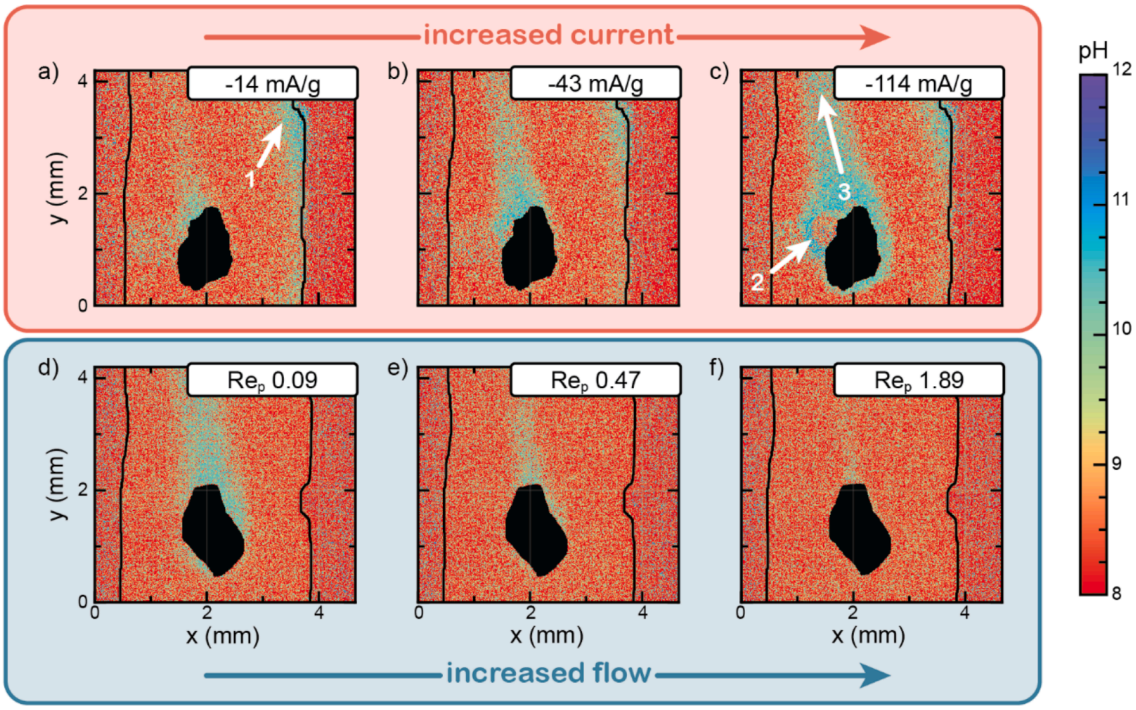

Fig. 4. Ph maps averaged over 20 images (20 s, 1 Hz) taken at steady state after 40 s of applying the relevant current density and flow velocity. The images show the influence of a-c) current density between −14 and −114 mA/g (−11 t0 −85 mA/cm^2) at a constant flow velocity (0.3 mm/s) with Re_p = 0.27, and the influence of d-f) flow velocity (Re_p) at a constant applied current density of −15 mA/g on the boundary layer thickness and plume formation. The arrows indicate 1. OH^- accumulation near the membrane, 2. Bubble formation, and 3. plume formation away from the membrane.

conversions demand high current densities to improve their economic viability, enhancing mass transfer by raising the flow velocity is a more attractive strategy.

We analyze the effects of current density and flow velocity on the diffusion boundary layer thickness along several rays in Fig. 5a and b, respectively. Although the diffusion boundary layer in Fig. 4a-c becomes more visible with increasing current density, the diffusion boundary layer thickness is independent of the current density for relatively horizontal rays (ray C, Fig. 5a). The higher visibility in Fig. 4c is merely caused by a steeper pH gradient within the boundary layer, while the thickness is actually the same as in Fig. 4a and b. This is in accordance with theory, which indicates that the boundary layer thickness is determined by the Sherwood number (Sh), which is related to Re_p and independent of the current density.

The situation is different for ray A (Fig. 5a), which points in the same direction as the flow. Here, the boundary layer thickness does show an increase with increasing current density. This is due to the larger amount of produced OH^- with increasing current density, which requires more mixing with bulk electrolyte to neutralize. This causes plume formation and a larger observed boundary layer in the direction A. Additionally, the high current density leads to the production of bubbles, and their detachment increases mixing and further enhances mixing in the boundary layer, which is shown for flow-by CO_2 electrolysis before [21]. Bubble formation was minimized in this study, to deconvolute the mixing effects and highlight the mixing potential of forced convection in 3D electrodes.

As mentioned, we expect a decrease in boundary layer thickness with increasing Re_p in Fig. 5b. This effect is slightly visible in two out of three analyzed regions (regions A and B), while the most horizontal region (region C) shows the opposite trend. This discrepancy is likely caused by the thin boundary layer with a relatively small OH^- concentration gradient inside it, or by the shape of the particle inducing a sideways electrolyte flow that carries OH^- ions in this direction. This combination makes our analysis less accurate, while the analysis in regions A and B is aided by the larger change in OH^- concentration. This effect should be more clearly present when operating at a higher current density.

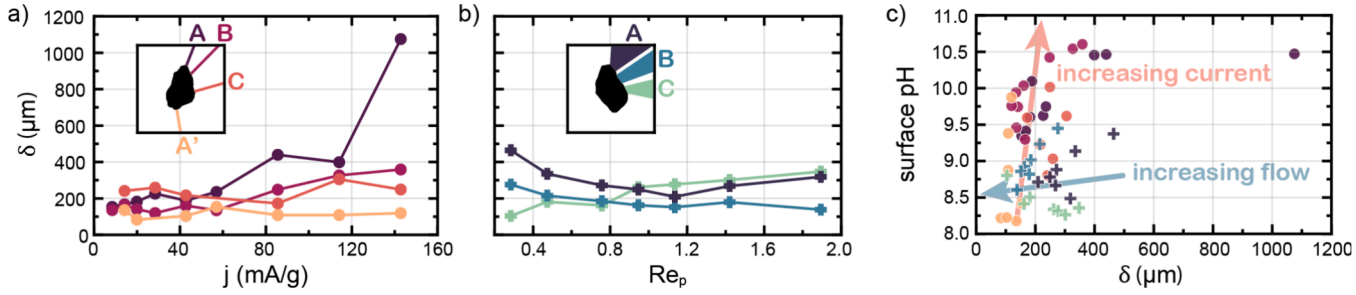

Fig. 5. Influence of a) current density (j) at a constant flow velocity of 0.3 mm/s (Re_p = 0.27), and b) the influence of flow velocity (Re_p) at a constant current density of −15 mA/g (−11 mA/cm^2) on the diffusion boundary layer thickness (δ) along various radial directions around a particle electrode. c) Shifts in δ and surface pH as a result of changing j and Re_p. For horizontal rays, raising the current density increases the surface pH with only a small effect on δ, while increasing the flow velocity decreases the δ at a mainly constant surface pH. For vertical rays, the δ and surface pH are also affected when increasing the current density and flow velocity, respectively.

We plot the pH close to the particle surface (average of the 5 first pixels on a ray) against the diffusion layer thickness in Fig. 5c to illustrate the different local reaction conditions that can be obtained for the conversion reaction by adjusting the applied current density and electrolyte flow velocity. Increasing the current clearly raises the surface pH, while increasing the flow decreases the diffusion boundary layer thickness and accelerates mass transfer from the bulk. We can use these observations to steer the local reaction conditions with current density and flow velocity.

Most electrochemical reactions benefit from fast mass transfer and an unaltered surface pH compared to the bulk, which corresponds to the region at the left bottom of Fig. 5c. However, other reactions may benefit from a slightly elevated pH or concentration of product close to the catalyst surface (left upper region in Fig. 5c), such as CO_2 reduction to higher carbon products (*i.e.*, in which the produced CO is converted to form C_{2+} products in a second step) [44,45]. In contrast, other reactions require a stable pH throughout the electrolyte to favor the desired reaction or to prevent detrimental effects on the catalyst (lower region of Fig. 5c) [46]. The current density and flow velocity, in combination with buffering electrolytes, can be used to steer the local environment towards the lower/upper region, or to the left/right side of the plot to achieve the optimum local reaction conditions.

3.2. Concentration profile near the particle

In more detail, we observe that the highest OH^- concentration is often not located at the electrode surface, but is located 100–200 μm away from the electrode surface instead (Fig. 3b). We constructed a simple model with a spherical particle electrode in COMSOL (Fig. 6d-f, see section 1.3 in the SI for model details) to verify that our observations are not caused by artefacts of the experimental method.

The 3D character of the cathode and the asymmetry imposed by the system geometry (*i.e.* anode on only one side) alter the concentration profile inside the diffusion boundary layer in two ways. First, the OH^- concentration on the left is considerably higher than on the side of the particle that is facing the anode, because of the electric field pulling the OH^- ions to the anode side of the channel. This compresses and concentrates the boundary layer on the left side, while it stretches and dilutes the diffusion layer on the anode side of the particle. This matches our previous observations of asymmetry. Secondly, the observed OH^- concentration profile on the anode facing side of the particle deviates from the profile that would be expected at a planar electrode. Instead, the OH^- concentration peaks further inside the diffusion boundary layer, as shown in Fig. 6b. This peak was observed in every experiment, as well as in the model (bottom row, Fig. 6) and is thus not caused by FLIM artefacts or the particle shape.

Increasing the current density raises the peak height in both the experiments and the model. The current density is increased by increasing the applied potential, which raises the electric field strength and accelerates migration, which shifts the peak location slighty away from the particle's surface as a result (Fig. 6b). This is also observed subtly in the simulations, in which the potential and current are adjusted to mimic the experiment (Fig. 6e). Furthermore, the peak shifts towards the particle and decreases slightly in height when increasing the flow velocity (Fig. 6c and f). In summary, the peak height is determined mainly by the current density through the OH^- production rate, while the peak location depends on the electric field strength through the migration velocity and on the flow velocity.

From these observations, we conclude that the peak is caused by OH^- that is produced at the bottom of the particle and flushed upwards along the curve of the particle electrode. More generally, the flow along a particle or an element of a 3D electrode will cause a convolution of concentration profiles produced upstream. The concentration profile observed at any location in the channel higher than the bottom of the particle will be an overlay of a series of gradients between the gradient caused by production at the observation height (which will have a high surface concentration and decreases to the bulk concentration) and the concentration gradient of all OH^- that is produced lower on the particle and flushed upwards. The current density controls how much OH^- is produced, but also determines the field strength, *i.e.* how fast the produced OH^- migrates towards the anode, and the flow velocity regulates how fast the OH^- is flushed upward and how much time it gets to migrate sideways before reaching the horizontal plane along which the profiles are recorded.

Hence, we conclude that this type of concentration profile is intrinsic for any electrode in flow in which the flow, diffusion, and migration

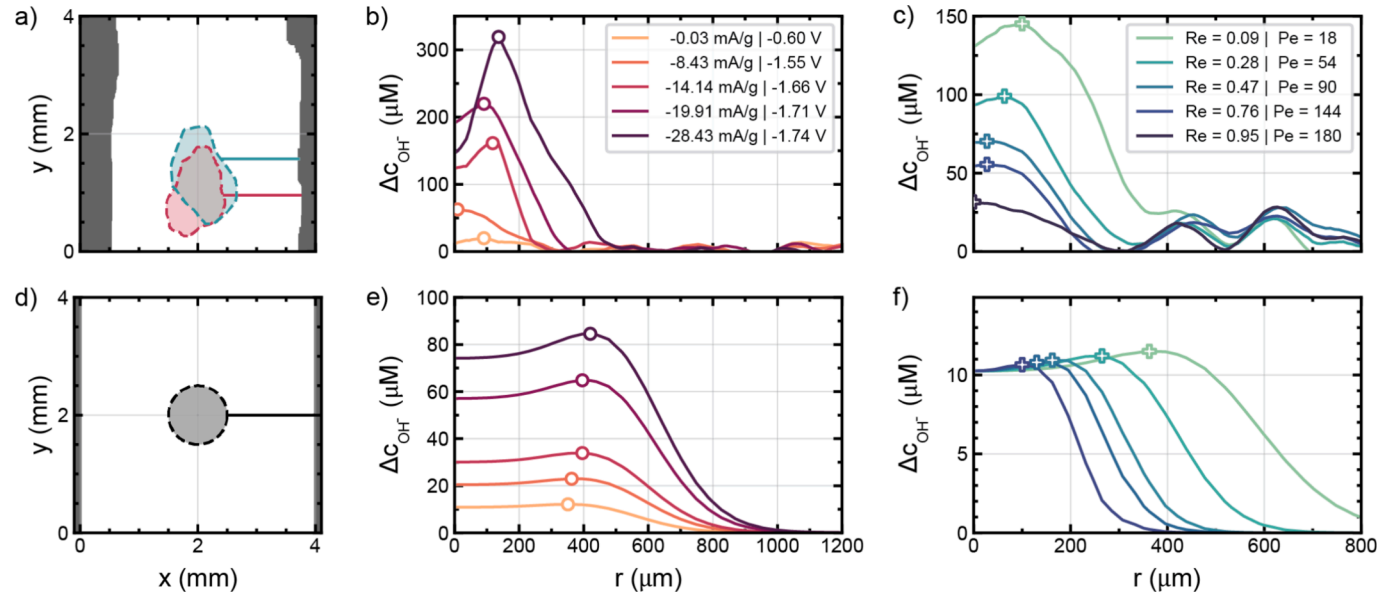

Fig. 6. Visualization of the OH^- concentration profiles in the experiments (top row) and model (bottom row) with markers indication the locations of the peak OH^- concentrations. Panels a) and d) show the shape of the particle used in each experiment (pink for the current density series, green for the flow velocity series, spherical in all simulations), and the horizontal plane next to the particle electrode along which the OH^- concentration profiles are plotted. Panels b) and e) show the influence of current density, and panels c) and f) show the influence of flow velocity. (For interpretation of the references to colour in this figure legend, the reader is referred to the web version of this article.)

directions do not align. This is certainly the case for non-planar electrodes in flow reactors, like flow-through and suspension electrodes. In the latter, the suspension particles have a non-zero velocity relative to the electrolyte as well, because of their difference in density with the electrolyte. We acknowledge that translating our findings to particles typically used in suspensions (usually 10–100 times smaller) presents challenges. While the aspect ratio of the boundary layer plumes are relatively insensitive to particle size in a laminar regime [47], the absolute values for the fluxes in migration, diffusion, and convection scale differently with particle size, complicating direct extrapolation of our results to different scales.

3.3. Capacitance-driven Faradaic reactions

In this section, we investigate how long the capacitance of the particle's large microscopic surface area can maintain an ongoing Faradaic reaction after contact with the current source is broken, which is of interest for suspension electrodes. We apply a constant potential to drive the HER and charge the electric double layer (EDL) during an "on" phase, and switch to the Open Circuit Potential (OCP) during an "off" phase after 3 min. We continue measuring the particle potential (Fig. 7a) and the surface pH (Fig. 7b) while the particle electrode discharges. Because the HER can be sustained as long as the particle potential is more negative than E^{eq}_{HER}, we derived the HER equilibrium potential (E^{eq}_{HER}) in real-time from the surface pH obtained with FLIM. Although the surface pH differs significantly during the "on"- and "off" phases, the E^{eq}_{HER} increases by less than 0.1 V (comparing the highest surface pH of 9 to the starting pH of 7.3). The complete range of calculated E^{eq}_{HER} values are indicated as a grey band in Fig. 7a. The HER can continue as long as the particle potential is more negative than this limit. In addition, the particle can perform the ORR as long as dissolved oxygen is present in the electrolyte because the E^{eq}_{ORR} lies 1.23 V above the E^{eq}_{HER} [48,49]. We performed the experiment at various charging potentials between −0.7 and −2.0 V vs SHE and we assess the influence of the charging potential on the surface pH and potential change over time in Fig. 7.

The surface pH (Fig. 7b) during charging increases with the charging potential because of the higher production rate of OH^-, and decays to the initial pH during the "off" phase as the produced OH^- ions are flushed away. However, the pH decay does not start immediately after switching to OCP and is always delayed by 5–10 s. It is hard to say whether this is caused by continued HER and ORR driven by the EDL capacitance, or by slow OH^--removal along the particle exterior. The cases that were charged at −1.7 and −2.0 V vs SHE show a significant peak in pH 10 s after switching to OCP. This peak is caused by the removal of bubbles, which interfere with the FLIM signal.

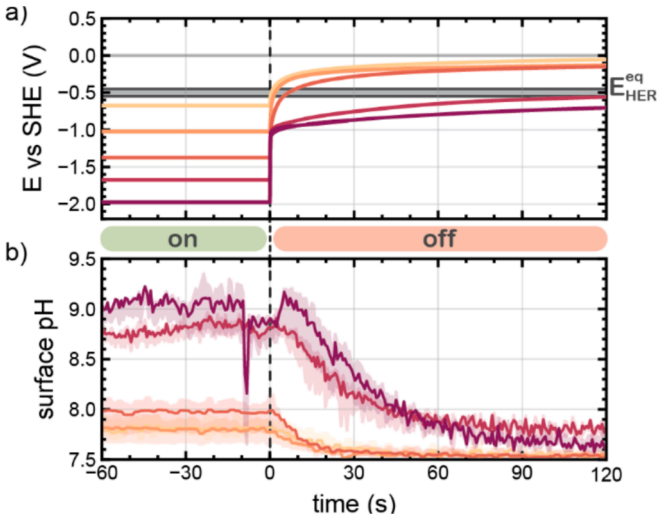

Fig. 7. a) Particle potential during the charging ("on" phase) at various potentials and after switching to Open Circuit Potential (OCP) ("off" phase), and the range of HER equilibrium potentials (E^{eq}_{HER}) calculated from the particle surface pH. b) Particle surface pH during the experiment, as obtained with FLIM.

The negative potential on the particle decays in two stages during the "off" stage in all cases (Fig. 7a). The first jump occurs almost instantly after switching to OCP, while the 2nd stage is significantly slower. The initial and fast potential change is caused by the sudden removal of Ohmic resistances when switching to OCP, whereas the subsequent gradual potential change is related to discharging the capacitive EDL. Changing the preceding charging potential alters the shape of the discharge curve in two ways: 1) The capacitive discharge after switching to OCP (between 0–120 s) is faster for small negative charging potentials than for large charging potentials. This may be because the EDL is not an ideal capacitor and the $Q(V)$ relation is not linear, resulting in a lower capacitance and steeper potential change with the dissipation of charges [50]. And 2) the graphs show discharge towards different values in two clusters, with those charged at −1.7 and −2.0 V approaching a more negative potential than those charged at −0.7, −1.0, and −1.4 V vs SHE, which quickly cross the equilibrium potential for HER. We suspect that this is determined by which reaction is performed on the particle. The potential in the three upper graphs (charged at −0.7, −1.0, and −1.4 V vs SHE) is likely too small for the HER. In that case, ORR is the only Faradaic reaction that can occur. The potential on the two lower graphs (charged at −1.7 and −2.0 V) is considerably larger and allows for both ORR and HER to occur simultaneously. Because the maximum O_2 concentration in water is only 1.1 mM, all available oxygen is instantly depleted at the electrode surface and hence, the discharge potential cannot surpass the HER limit for at least 120 s.

Regardless of which Faradaic reaction is occurring, we observe a continued discharge of the capacitive EDL after switching to OCP, during which sufficiently negative potentials to drive either the HER or the ORR are maintained for at least 2 min. This suggests that the particle capacitance can indeed sustain a Faradaic reaction for a while after contact with a current source is broken, albeit at a lower current density than when a potential is applied (deduced from the decreasing surface pH in Fig. 7b). We will now assess the contributions of the different mechanisms and the timescales at which they occur in more detail.

We study the potential curves further because the pH profiles (Fig. 7b) do not distinguish between slow OH^- removal by flushing or continued OH^- production through HER driven by the EDL capacitance as the possible causes for the delayed pH decay in the FLIM results after ending the "on" phase.

Self-discharge of EDL capacitors (EDLCs) is known to occur through Faradaic reactions, charge redistribution, and current leakage. First of all, Faradaic reactions can take place whenever the potential on the electrode is sufficient to cause electron transfer for a redox reaction. The electron transfer from the electrode is accompanied by the release of ions from the EDL and a loss of cell voltage [51]. Secondly, charge redistribution is caused by a difference in charging speed between different parts of the electrode due to differences in resistance. For example, the outer surface area is easier to access for ions in solution than internal structures such as pores, which leads to faster charging of the EDL on the outer surface area. Ultimately, this results in an uneven distribution of charges throughout the material and a larger potential at the outer surface, where the potential is measured [51,52]. Upon switching to the "off" phase, the measured potential becomes smaller as the charges slowly redistribute to achieve an even charge distribution throughout the material. Finally, current leakage is a common problem when the capacitor electrodes are separated by a membrane or porous separator. Such separators allow for ion transfer between the compartments, effectively creating yet another discharge pathway [36,51].

Combining these three mechanisms, the self-discharge of an EDLC through these processes can be described by [41]

$$\Delta E(t) = a\left(1 - \exp\left(\frac{-t}{\tau}\right)\right) + b\ln(t) + c\sqrt{t} \quad (3)$$

in which ΔE is the change in potential compared to the "on" phase, t is the time after switching off the potential control, τ is a characteristic time constant, and a, b, and c are constants. The first term describes the potential loss due to electrolytic current leakage and ohmic resistances, the second term corresponds to the Faradaic contribution, and the third term is related to diffusion-controlled processes, which includes diffusion-limited Faradaic reactions and charge redistribution.[41] We obtained the total discharge contributions of these three terms over time by fitting the discharge curves to the equation.

The first term, related to current leakage and ohmic resistances, causes the potential jump upon switching off the potential control (at $t = 0$), due to nullifying the current (i) in Ohm's law ($E = iR$). The data fitting shows that the current leakage is significantly smaller than the ohmic drop, causing the grey area in Fig. 8a-c to remain constant over time. The contributions of other self-discharge mechanisms are highly dependent on the charging potential. The purely Faradaic contribution decreases visibly with increasingly negative charging potentials of −1.4, −1.7, and −2.0 V vs SHE (Fig. 8 a-c). Charge redistribution and mass transfer limitations in the Faradaic charge transfer gain importance at these larger applied potentials and currents, causing the discharging behavior to become more diffusion-controlled. For less negative charging potentials (−0.7 and −1.0 V vs SHE), the Faradaic contribution is smaller than that for −1.4 V vs SHE.

To understand why the Faradaic contribution peaks at −1.4 V vs SHE, and is smaller for both larger and smaller charging potentials, we translate the contributions to ΔE into a current density. Assuming ideal capacity behavior (*i.e.*, constant capacitance), the slope $\frac{d\Delta E}{dt}$ is proportional to the current density for each mechanism. Hence, the slopes of the Faradaic charge transfer and diffusion-controlled discharge curves (Fig. 8 d-e) give an indication of the intensity and timescale at which each mechanism occurs. The purely Faradaic potential change is fastest and it is maintained longest (>20 s) after charging at −1.4 V vs SHE. The estimated discharge current that is entirely Faradaic is smaller and ceases within a few seconds when charging at a larger (−1.7 and −2.0 V) or smaller (−0.7 and −1.0 V vs SHE) potentials (Fig. 8d). This difference may be caused by either 1) a smaller overpotential (in the case of charging at −0.7 and −1.0 V vs SHE), or 2) depletion of oxygen (at −1.7 and −2.0 V vs SHE). For the large charging potentials (at −1.7 and −2.0 V vs SHE), oxygen may be depleted before and after switching off the potential control, which results in a high contribution for diffusion-controlled discharge instead. Alternatively, charge redistribution may play a substantial role at larger charging potentials. We cannot discriminate between these two effects, as both invoke a shift towards diffusion-controlled discharge at the increasingly large charging potentials in Fig. 8e.

Therefore, the charging potential should be optimized when using a suspension electrode for a Faradaic reaction. In this case, it is important for the capacitance of the porous particles to drive the reaction long enough to bridge their non-contact time with a current source. The applied potential should be large enough to provide sufficient overpotential and make the reaction last longer, but small enough to avoid significant diffusion limitations and charge redistribution. Ideally, charge redistribution can be minimized by charging the system for longer periods, which allows for more even charge distribution. However, to further suppress redistribution, the design of the current collector and the suspension should aim to reduce the non-contact time between the electrodes and the current source, ensuring more continuous current flow.

4. Conclusions

Poor mass transfer at high operating current densities can cause an unfavorable local reaction environment near electrodes and affect selectivity and stability negatively in many electrochemical technologies. We studied the pH profiles during water electrolysis with FLIM around an activated carbon (AC) particle electrode, representing an element of a 3D electrode. The obtained pH gradients give an estimate of the diffusion boundary layer thickness and the severity of plume formation, and indicate the extent of reactant depletion or product accumulation near the electrode.

The 3D character of the electrode and the asymmetry of the system lead to the formation of an asymmetrical diffusion boundary layer with an OH^- concentration profile that deviates from the linear profile known from planar electrodes. The OH^- gradient spanned over a thickness of 100 – 600 μm to the side, and a larger distance in the direction of applied electrolyte flow to create an OH^--rich plume. We show that the

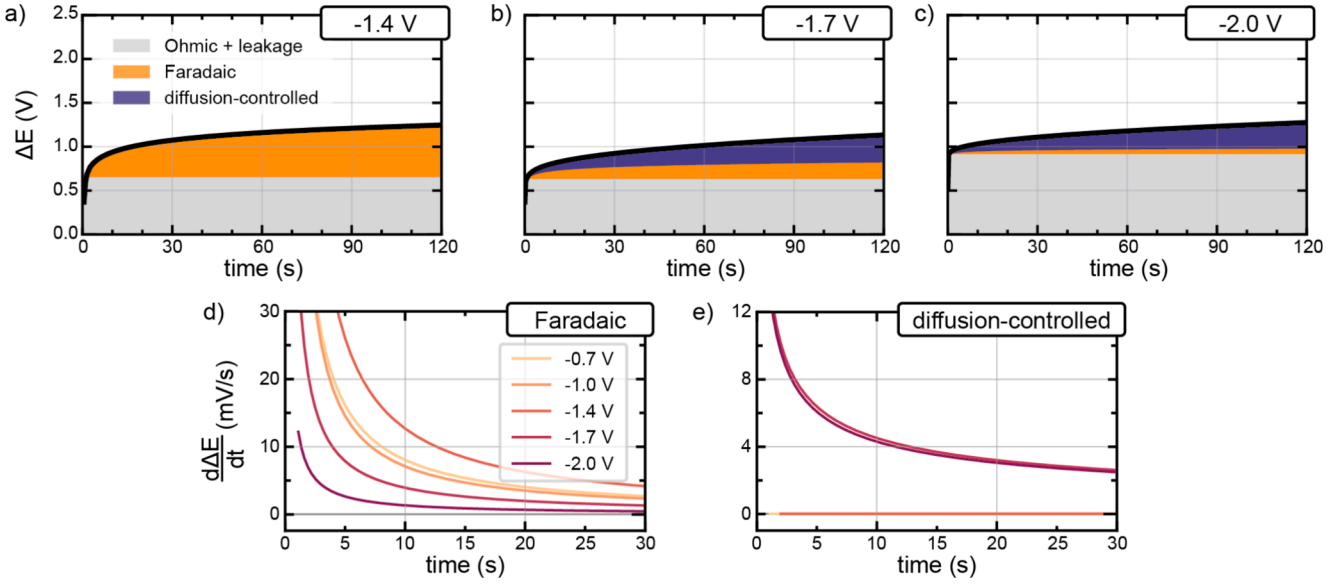

Fig. 8. Panels a-c) show the contributions of the different discharge mechanisms on the potential change (ΔE) over time after charging at a) −1.4, b) −1.7, and c) −2.0 V vs SHE. The charging potential influences which discharge behavior is more dominant. Faradaic charge transfer dominates at small charging potential (−1.4 V vs SHE), and diffusion limitations that can also increase charge redistribution gain importance at larger charging potential (−2.0 V vs SHE). Panels d) and e) show the discharging rates $\frac{d\Delta E}{dt}$ attributed to purely Faradaic charge transfer (d) and diffusion-controlled processes (e).

boundary layer thickness and plume size are most effectively decreased by an increase in flow velocity, while the surface pH is increased at higher current density. This implies that the 3D electrode design (*e.g.* pore size and shape) and flow velocity can be adapted to improve the reaction environment on the microscale, as well as on the macroscale by ensuring sufficient plume dissipation and preventing increased reagent depletion and product accumulation at the electrode surface or higher up in the electrode at required current densities.

Additionally, we investigated how long the capacitance of an AC particle can drive a Faradaic reaction after interrupting the potential control, by fitting the discharge curve to a self-discharge model for EDLCs. We conclude that our capacitive particle, representing a suspension electrode particle, can drive Faradaic reactions after interrupting the potential control, but probably drives ORR instead of HER in our case. We demonstrate that an optimum charging potential exists (in our case −1.4 V vs SHE) to provide sufficient overpotential, while avoiding the diffusion-limited regime and charge redistribution.

In this study, FLIM has proven to be a valuable tool for studying hydrodynamics and local concentrations around 3D electrodes at high spatial and time resolution. While our findings provide insights into the behavior of 3D electrodes and the hydroxide boundary layer during electrochemical reactions, further research is needed to fully understand the implications for electrode design across various applications. Our observations suggest potential avenues for optimizing electrode morphology and flow conditions to mitigate negative effects caused by high current densities and plume formation to improve local reaction environment, but additional experimental work would be required to validate these hypotheses across a wider range of electrochemical systems.

Funding sources

This project has received funding from the European Research Council (ERC) under the European Union's Horizon 2020 research and innovation programme (Grant agreement No 852115). This work reflects the authors' view and the ERC Executive Agency is not responsible for any use resulting from the information it contains.

CRediT authorship contribution statement

Nathalie E.G. Ligthart: Writing – original draft, Visualization, Methodology, Investigation, Formal analysis, Conceptualization. **Julius Sommer:** Writing – original draft, Visualization, Methodology, Investigation, Formal analysis, Conceptualization. **Jorrit Bleeker:** Writing – review & editing, Methodology. **Lorenz M. Baumgartner:** Writing – review & editing, Methodology. **Johan T. Padding:** Writing – review & editing, Supervision. **David A. Vermaas:** Writing – review & editing, Supervision, Methodology, Funding acquisition.

Declaration of competing interest

The authors declare that they have no known competing financial interests or personal relationships that could have appeared to influence the work reported in this paper.

Acknowledgments

The authors thank Wolter Jager for developing and synthesizing the quinolinium-based dye, and Christiaan Schinkel and Aron Kahn for developing the FLIM setup.

Appendix A. Supplementary data

The Supporting Information contains: more detailed description of the methods, including illustrations of the flow cell and setup, and a detailed description of the image analysis and modelling methods; additional results including potential data, FLIM images, and graphs. Supplementary data to this article can be found online at https://doi.org/10.1016/j.cej.2025.160474.

Data availability

The relevant data is available in the Zenodo repository at DOI https://doi.org/10.5281/zenodo.12683346.

References

[1] G. Centi, G. Iaquaniello, S. Perathoner, Chemical engineering role in the use of renewable energy and alternative carbon sources in chemical production, BMC Chem. Eng. 1 (2019) 5, https://doi.org/10.1186/s42480-019-0006-8.
[2] G. Hammond, M. Newborough, Glasgow climate pact: A step on the way towards a lower carbon dioxide world, Proc. Inst. Civ. Eng. - Civ. Eng. 175 (2022) 8, https://doi.org/10.1680/jcien.2022.175.1.8.
[3] A. Otto, T. Grube, S. Schiebahn, D. Stolten, Closing the loop: captured CO2 as a feedstock in the chemical industry, Energy Environ. Sci. 8 (2015) 3283–3297, https://doi.org/10.1039/C5EE02591E.
[4] P. De Luna, C. Hahn, D. Higgins, S.A. Jaffer, T.F. Jaramillo, E.H. Sargent, What would it take for renewably powered electrosynthesis to displace petrochemical processes? Science 364 (2019) eaav3506 https://doi.org/10.1126/science.aav3506.
[5] M. Jouny, W. Luc, F. Jiao, General techno-economic analysis of CO2 electrolysis systems, Ind. Eng. Chem. Res. 57 (2018) 2165–2177, https://doi.org/10.1021/acs.iecr.7b03514.
[6] D. Agrawal, N. Mahajan, S.A. Singh, I. Sreedhar, Green hydrogen production pathways for sustainable future with net zero emissions, Fuel 359 (2024) 130131, https://doi.org/10.1016/j.fuel.2023.130131.
[7] S. Sebastian, S. Wijewardane, S. Srinivasan, Recent advances in hydrogen production, storage, and fuel cell Technologies with an emphasis on inventions, innovations, and commercialization, Sol. Compass 8 (2023) 100065, https://doi.org/10.1016/j.solcom.2023.100065.
[8] Y. Oh, H. Vrubel, S. Guidoux, X. Hu, Electrochemical reduction of CO2 in organic solvents catalyzed by MoO2, Chem. Commun. 50 (2014) 3878–3881, https://doi.org/10.1039/C3CC49262A.
[9] N.J. Matteucci, C.T. Mallia, B.J. Neyhouse, M.V. Majji, F.R. Brushett, Toward electrochemical design principles of redox-mediated flow batteries, Curr. Opin. Electrochem. 42 (2023) 101380, https://doi.org/10.1016/j.coelec.2023.101380.
[10] H. Chen, Y. Liu, X. Zhang, Q. Lan, Y. Chu, Y. Li, Q. Wu, Single-component slurry based lithium-ion flow battery with 3D current collectors, J. Power Sources 485 (2021) 229319, https://doi.org/10.1016/j.jpowsour.2020.229319.
[11] R. Sharifian, R.M. Wagterveld, I.A. Digdaya, C. Xiang, D.A. Vermaas, Electrochemical carbon dioxide capture to close the carbon cycle, Energy Environ. Sci. 14 (2021) 781–814, https://doi.org/10.1039/D0EE03382K.
[12] D.W. Keith, G. Holmes, D. St, K.H. Angelo, A process for capturing CO2 from the atmosphere, Joule 2 (2018) 1573–1594, https://doi.org/10.1016/j.joule.2018.05.006.
[13] C.A. Martínez-Huitle, M. Panizza, Electrochemical oxidation of organic pollutants for wastewater treatment, Curr. Opin. Electrochem. 11 (2018) 62–71, https://doi.org/10.1016/j.coelec.2018.07.010.
[14] M.E. Suss, S. Porada, X. Sun, P.M. Biesheuvel, J. Yoon, V. Presser, Water desalination via capacitive deionization: what is it and what can we expect from it? Energy Environ. Sci. 8 (2015) 2296–2319, https://doi.org/10.1039/C5EE00519A.
[15] S. Porada, R. Zhao, A. van der Wal, V. Presser, P.M. Biesheuvel, Review on the science and technology of water desalination by capacitive deionization, Prog. Mater. Sci. 58 (2013) 1388–1442, https://doi.org/10.1016/j.pmatsci.2013.03.005.
[16] M. Vanoppen, E. Criel, G. Walpot, D.A. Vermaas, A. Verliefde, Assisted reverse electrodialysis—principles, mechanisms, and potential, npj Clean Water 1 (2018) 1–5, https://doi.org/10.1038/s41545-018-0010-1.
[17] D.M. Weekes, D.A. Salvatore, A. Reyes, A. Huang, C.P. Berlinguette, Electrolytic CO2 reduction in a flow cell, Acc. Chem. Res. 51 (2018) 910–918, https://doi.org/10.1021/acs.accounts.8b00010.
[18] G. Marcandalli, M.C.O. Monteiro, A. Goyal, M.T.M. Koper, Electrolyte effects on CO2 electrochemical reduction to CO, Acc. Chem. Res. 55 (2022) 1900–1911, https://doi.org/10.1021/acs.accounts.2c00080.
[19] S. Garg, M. Li, A.Z. Weber, L. Ge, L. Li, V. Rudolph, G. Wang, T.E. Rufford, Advances and challenges in electrochemical CO2 reduction processes: an engineering and design perspective looking beyond new catalyst materials, J. Mater. Chem. A 8 (2020) 1511–1544, https://doi.org/10.1039/C9TA13298H.
[20] M.C.O. Monteiro, A. Mirabal, L. Jacobse, K. Doblhoff-Dier, S.C. Barton, M.T. M. Koper, Time-resolved local pH measurements during CO2 reduction using scanning electrochemical microscopy: buffering and tip effects, JACS Au 1 (2021) 1915–1924, https://doi.org/10.1021/jacsau.1c00289.
[21] L.M. Baumgartner, A. Kahn, M. Hoogland, J. Bleeker, W.F. Jager, D.A. Vermaas, Direct imaging of local pH reveals bubble-induced mixing in a CO2 electrolyzer, ACS Sustain. Chem. Eng. 11 (2023) 10430–10440, https://doi.org/10.1021/acssuschemeng.3c01773.
[22] S. Brosch, F. Wiesner, A. Decker, J. Linkhorst, M. Wessling, Spatio-temporal electrowetting and reaction monitoring in microfluidic gas diffusion electrode

elucidates mass transport limitations, Small Weinh. Bergstr. Ger. 20 (2024) e2310427, https://doi.org/10.1002/smll.202310427.
[23] J.W. Blake, J.T. Padding, J.W. Haverkort, Analytical modelling of CO2 reduction in gas-diffusion electrode catalyst layers, Electrochim. Acta 393 (2021) 138987, https://doi.org/10.1016/j.electacta.2021.138987.
[24] R. Kas, A.G. Star, K. Yang, T. Van Cleve, K.C. Neyerlin, W.A. Smith, Along the channel gradients impact on the spatioactivity of gas diffusion electrodes at high conversions during CO2 electroreduction, ACS Sustain. Chem. Eng. 9 (2021) 1286–1296, https://doi.org/10.1021/acssuschemeng.0c07694.
[25] A.A. Wong, S.M. Rubinstein, M.J. Aziz, Direct visualization of electrochemical reactions and heterogeneous transport within porous electrodes *in operando* by fluorescence microscopy, Cell Rep. Phys. Sci. 2 (2021) 100388, https://doi.org/10.1016/j.xcrp.2021.100388.
[26] X. Lu, C. Zhou, R.S. Delima, E.W. Lees, A. Soni, D.J. Dvorak, S. Ren, T. Ji, A. Bahi, F. Ko, C.P. Berlinguette, Visualization of CO2 electrolysis using optical coherence tomography, Nat. Chem. 16 (2024) 979–987, https://doi.org/10.1038/s41557-024-01465-5.
[27] A. Böhme, J.C. Bui, A.Q. Fenwick, R. Bhide, C.N. Feltenberger, A.J. Welch, A. J. King, A.T. Bell, A.Z. Weber, S. Ardo, H.A. Atwater, Direct observation of the local microenvironment in inhomogeneous CO2 reduction gas diffusion electrodes via versatile pOH imaging, Energy Environ. Sci. 16 (2023) 1783–1795, https://doi.org/10.1039/D2EE02607D.
[28] B.K. Chakrabarti, E. Kalamaras, A.K. Singh, A. Bertei, J. Rubio-Garcia, V. Yufit, K. M. Tenny, B. Wu, F. Tariq, Y.S. Hajimolana, N.P. Brandon, C.T.J. Low, E.P. L. Roberts, Y.-M. Chiang, F.R. Brushett, Modelling of redox flow battery electrode processes at a range of length scales: a review, Sustain. Energy Fuels 4 (2020) 5433–5468, https://doi.org/10.1039/D0SE00667J.
[29] J.W. Haverkort, A theoretical analysis of the optimal electrode thickness and porosity, Electrochim. Acta 295 (2019) 846–860, https://doi.org/10.1016/j.electacta.2018.10.065.
[30] M.S. Isaacson, A.A. Sonin, Sherwood number and friction factor correlations for electrodialysis systems, with application to process optimization, Ind. Eng. Chem. Process Des. Dev. 15 (1976) 313–321, https://doi.org/10.1021/i260058a017.
[31] H. Rajaei, A. Rajora, J.W. Haverkort, Design of membraneless gas-evolving flow-through porous electrodes, J. Power Sources 491 (2021) 229364, https://doi.org/10.1016/j.jpowsour.2020.229364.
[32] G. Wen, B. Ren, X. Wang, D. Luo, H. Dou, Y. Zheng, R. Gao, J. Gostick, A. Yu, Z. Chen, Continuous CO2 electrolysis using a CO2 exsolution-induced flow cell, Nat. Energy 7 (2022) 978–988, https://doi.org/10.1038/s41560-022-01130-6.
[33] C. Zhang, J. Ma, L. Wu, J. Sun, L. Wang, T. Li, T.D. Waite, Flow electrode capacitive deionization (FCDI): recent developments, environmental applications, and future perspectives, Environ. Sci. Technol. 55 (2021) 4243–4267, https://doi.org/10.1021/acs.est.0c06552.
[34] A. Rommerskirchen, A. Kalde, C.J. Linnartz, L. Bongers, G. Linz, M. Wessling, Unraveling charge transport in carbon flow-electrodes: Performance prediction for desalination applications, Carbon 145 (2019) 507–520, https://doi.org/10.1016/j.carbon.2019.01.053.
[35] M. Mourshed, S.M.R. Niya, R. Ojha, G. Rosengarten, J. Andrews, B. Shabani, Carbon-based slurry electrodes for energy storage and power supply systems, Energy Storage Mater. 40 (2021) 461–489, https://doi.org/10.1016/j.ensm.2021.05.032.
[36] V. Presser, C.R. Dennison, J. Campos, K.W. Knehr, E.C. Kumbur, Y. Gogotsi, The electrochemical flow capacitor: A new concept for rapid energy storage and recovery, Adv. Energy Mater. 2 (2012) 895–902, https://doi.org/10.1002/aenm.201100768.
[37] L. Amit, D. Naar, R. Gloukhovski, G.J. la O', M.E. Suss, A single-flow battery with multiphase flow, ChemSusChem 14 (2021) 1068–1073, https://doi.org/10.1002/cssc.202002135.
[38] C. Borsje, T. Sleutels, W. Zhang, W. Feng, C.J.N. Buisman, A. ter Heijne, Making the best use of capacitive current: Comparison between fixed and moving granular bioanodes, J. Power Sources 489 (2021) 229453, https://doi.org/10.1016/j.jpowsour.2021.229453.
[39] A. Deeke, T.H.J.A. Sleutels, T.F.W. Donkers, H.V.M. Hamelers, C.J.N. Buisman, A. Ter Heijne, Fluidized capacitive bioanode as a novel reactor concept for the microbial fuel cell, Environ. Sci. Technol. 49 (2015) 1929–1935, https://doi.org/10.1021/es503063n.
[40] J. Bleeker, A.P. Kahn, L.M. Baumgartner, F.C. Grozema, D.A. Vermaas, W.F. Jager, Quinolinium-based fluorescent probes for dynamic ph monitoring in aqueous media at high pH using fluorescence lifetime imaging, ACS Sens. (2023), https://doi.org/10.1021/acssensors.3c00316.
[41] A. Lewandowski, P. Jakobczyk, M. Galiński, M. Biegun, Self-discharge of electrochemical double layer capacitors, Phys. Chem. Chem. Phys. PCCP 15 (2013), https://doi.org/10.1039/c3cp44612c.
[42] N.E.G. Ligthart, G.P. Vergel, J.T. Padding, D.A. Vermaas, Practical potential of suspension electrodes for enhanced limiting currents in electrochemical CO2 reduction, Energy Adv. 3 (2024) 841–853, https://doi.org/10.1039/D3YA00611E.
[43] M. Kraume, Transportvorgänge in der Verfahrenstechnik: Grundlagen und apparative Umsetzungen, Springer Vieweg, Berlin [Heidelberg], 2020, 3. Auflage, 10.1007/978-3-662-60012-2.
[44] D. Gurudayal, S. Perone, Y. Malani, S. Lum, J.W. Haussener, Ager, sequential cascade electrocatalytic conversion of carbon dioxide to C–C coupled products, ACS Appl. Energy Mater. 2 (2019) 4551–4559, https://doi.org/10.1021/acsaem.9b00791.
[45] X. Liu, P. Schlexer, J. Xiao, Y. Ji, L. Wang, R.B. Sandberg, M. Tang, K.S. Brown, H. Peng, S. Ringe, C. Hahn, T.F. Jaramillo, J.K. Nørskov, K. Chan, pH effects on the electrochemical reduction of CO(2) towards C2 products on stepped copper, Nat. Commun. 10 (2019) 32, https://doi.org/10.1038/s41467-018-07970-9.
[46] N. Govindarajan, A. Xu, K. Chan, How pH affects electrochemical processes, Science 375 (2022) 379–380, https://doi.org/10.1126/science.abj2421.
[47] E. Moses, G. Zocchi, A. Libchaberii, An experimental study of laminar plumes, J. Fluid Mech. 251 (1993) 581–601, https://doi.org/10.1017/S0022112093003532.
[48] C. Borsje, T. Sleutels, C.J.N. Buisman, A. ter Heijne, Improving the discharge of capacitive granules in a moving bed reactor, J. Environ. Chem. Eng. 9 (2021) 105556, https://doi.org/10.1016/j.jece.2021.105556.
[49] A.M. Oickle, H.A. Andreas, Examination of water electrolysis and oxygen reduction as self-discharge mechanisms for carbon-based, aqueous electrolyte electrochemical capacitors, J. Phys. Chem. C 115 (2011) 4283–4288, https://doi.org/10.1021/jp1067439.
[50] A.A. Moya, Nonlinear charge-voltage relationships in electric double layer capacitors performing under constant load resistance, J. Energy Storage 71 (2023) 108136, https://doi.org/10.1016/j.est.2023.108136.
[51] H.A. Andreas, Self-discharge in electrochemical capacitors: a perspective article, J. Electrochem. Soc. 162 (2015) A5047, https://doi.org/10.1149/2.0081505jes.
[52] H.A. Andreas, J.M. Black, A.A. Oickle, Self-discharge in manganese oxide electrochemical capacitor electrodes in aqueous electrolytes with comparisons to faradaic and charge redistribution models, Electrochim. Acta 140 (2014) 116–124, https://doi.org/10.1016/j.electacta.2014.03.104.